

RiemanLine: Riemannian Manifold Representation of 3D Lines for Factor Graph Optimization

Yanyan Li¹, Ze Yang², Keisuke Tateno³, Federico Tombari^{3,4}, Liang Zhao⁵, Gim Hee Lee¹

¹National University of Singapore

²Peking University

³Google

⁴Technical University of Munich

⁵The University of Edinburgh

Abstract

Minimal parametrization of 3D lines plays a critical role in camera localization and structural mapping. Existing representations in robotics and computer vision predominantly handle independent lines, overlooking structural regularities such as sets of parallel lines that are pervasive in man-made environments. This paper introduces **RiemanLine**, a unified minimal representation for 3D lines formulated on Riemannian manifolds that jointly accommodates both individual lines and parallel-line groups. Our key idea is to decouple each line landmark into global and local components: a shared vanishing direction optimized on the unit sphere S^2 , and scaled normal vectors constrained on orthogonal subspaces, enabling compact encoding of structural regularities. For n parallel lines, the proposed representation reduces the parameter space from $4n$ (orthonormal form) to $2n + 2$, naturally embedding parallelism without explicit constraints. We further integrate this parameterization into a factor graph framework, allowing global direction alignment and local reprojection optimization within a unified manifold-based bundle adjustment. Extensive experiments on ICL-NUIM, TartanAir, and synthetic benchmarks demonstrate that our method achieves significantly more accurate pose estimation and line reconstruction, while reducing parameter dimensionality and improving convergence stability.

Code — <https://github.com/yanyan-li/RiemanLine>

1 Introduction

Robustly reconstructing (Schonberger and Frahm 2016; Forster, Pizzoli, and Scaramuzza 2014) unknown three-dimensional scenes and estimating (Carlone et al. 2015; Carlone and Calafiore 2018) six degrees-of-freedom (6-DoF) camera poses from visual inputs are fundamental challenges in robotics and computer vision. However, these odometry and SLAM methods systems often suffer from structural inaccuracies and pose drift during the incremental camera tracking and mapping process. To mitigate these issues, techniques such as local bundle adjustment (Mur-Artal, Montiel, and Tardos 2015; Rosinol et al. 2020), sliding window optimization (Qin, Li, and Shen 2018; Engel, Koltun, and Cremers 2017), and loop closure (Labbé and Michaud 2019; Mur-Artal, Montiel, and Tardos 2015) are commonly incorporated. The core of these techniques lies in

Under Review

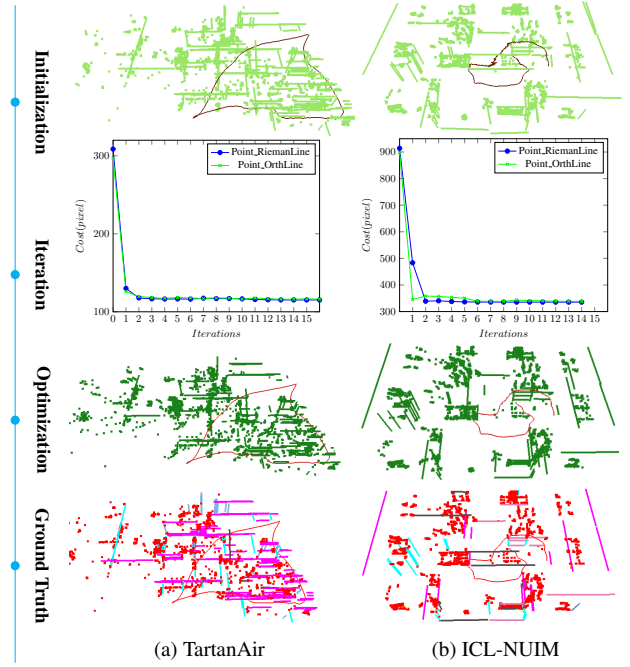


Figure 1: An illustration of co-visibility factor graph optimization based on points and lines. The initial factor graphs are depicted in the first row, with landmarks and trajectories colored light green and scarlet, respectively. The convergence curves for different representations are plotted in the second row. The optimized results based on the proposed *Point-RiemanLine* method and ground-truth graphs are presented in the last rows, respectively.

the use of factor graph optimization (Carlone and Calafiore 2018), which jointly refines the structure and transformation parameters. In this paper, we present a novel solution to the line-leveraged factor graph optimization problem by proposing a compact line parameterization on a Riemannian manifold along with constraint factors that connect line landmarks to camera poses, as shown in Figure 1.

Point features have long served as the foundation for most visual pose estimation systems, as demonstrated by their widespread adoption in leading methods (Mur-Artal,

Montiel, and Tardos 2015; Qin, Li, and Shen 2018; Rosinol et al. 2020). Despite their success, point features exhibit notable limitations, especially in challenging environments such as indoor scenes. To overcome the limitations of point-only factor graph optimization (Li et al. 2024), recent efforts have explored the integration of additional geometric primitives such as lines (Lu and Song 2015; Zuo et al. 2017) and planes (Zhou, Koppel, and Kaess 2021) into both tracking and optimization modules. Compared to plane detection which is typically based on depth maps (Salas-Moreno et al. 2014) or convolutional neural networks (Paigwar et al. 2020), line features can be efficiently extracted from RGB images, offering a versatile and computationally efficient means to enhance visual odometry performance. The most popular and widely adopted line parameterization method in line-based SLAM systems is the **Orthonormal algorithm** (Bartoli and Sturm 2005), which enables elegant optimization within the framework of **Lie Algebra**.

Typically, a single line segment contributes a re-projection factor (Hartley and Zisserman 2003) to the optimization module, whereas a collection of lines imparts broader structural and global regularities. Specifically, a group of parallel line segments on a 2D image plane crosses at the vanishing point, which can be projected to the camera coordinate to obtain the corresponding vanishing direction (McLean and Kotturi 1995) via a related intrinsic matrix. A group of vanishing direction vectors can model structured environments such as the Atlanta or Manhattan World assumptions (Straub et al. 2017). However, these assumptions are often too restrictive for general environments, and it is also difficult to optimize the structure as one primitive in factor graph optimization modules. Furthermore, conventional minimal parameterization (Bartoli and Sturm 2005) that is widely adopted in line-SLAM systems (Zuo et al. 2017; He et al. 2018) lacks the expressiveness to compactly parametrize a group of structure lines. Consequently, this leads to increased complexity and reduced efficiency since the optimization frameworks must rely on additional parameters and manually introduce constraints into loss functions to capture the relationships among these lines.

In this paper, we first propose a unified minimal representation for 3D lines, including individual and structure line landmarks, which has a clear geometric interpretation in representation and optimization based on Riemannian manifolds. Specifically, the line parameters are explicitly decoupled into **global** and **local** components: the global component defines the shared direction of parallel lines, and the local component that lies in the orthogonal plane encodes scaled normals that distinguish each line. Representing n parallel 3D lines with the Orthonormal representation requires $4n$ parameters. In contrast, our method reduces this to only $2n + 2$ parameters, significantly reducing the dimensionality while implicitly encoding parallelism without additional constraints. We integrate this representation into a joint factor graph framework with co-visibility factors, enabling both accurate pose estimation and structurally consistent line reconstruction. Our contributions are summarized as follows:

- We introduce a unified minimal parameterization for 3D

Algorithm	Parameters
Euclidean	$\mathbf{P}_s, \mathbf{P}_e$ endpoints of the 3D line
Plücker	\mathbf{n}, \mathbf{v} $\mathbf{n} = [\mathbf{P}_s]_{\times} \mathbf{P}_e, \mathbf{v} = \mathbf{P}_s - \mathbf{P}_e$
Quaternion	$\bar{\mathbf{q}}, d$ $\mathcal{R}(\bar{\mathbf{q}}) = [\mathbf{n} \ \mathbf{v} \ [\mathbf{n}]_{\times} \mathbf{v}], d = \ \mathbf{n}\ /\ \mathbf{v}\ $
Closest Point	$\mathbf{j} = d\bar{\mathbf{q}}$
Spherical	θ, ϕ, α, d θ, ϕ , and α are angles, d is the distance

Table 1: Popular line representations and transformation relationships between them. Here $[\cdot]_{\times}$ is the skew-s operation, and the \mathcal{R} is the transformation operation from quaternion to rotation matrix. The definitions of the remaining parameters are provided in Section 3.

lines on Riemannian manifolds that seamlessly extends from independent lines to sets of parallel lines by explicitly decoupling global and local components.

- A joint factor graph framework incorporating co-visibility and extensibility factors, specifically designed to leverage the proposed minimal representation;
- We conduct extensive evaluations on ICL-NUIM, TantanAir, and synthetic datasets, demonstrating that our method achieves higher accuracy with fewer parameters and improved convergence stability compared to existing representations.

2 Related work

As shown in Table 1, two stages of representation are typically involved in landmark reconstruction and optimization tasks (Bartoli and Sturm 2005). The first stage focuses on 3D triangulation from 2D measurements, and the second seeks a minimal parametrization for iterative refinement. The two stages can be unified into a single step when the degrees of freedom used in reconstruction meet the requirements of minimal parametrization.

Generally, Euclidean XYZ (Mur-Artal, Montiel, and Tardos 2015; Qin, Li, and Shen 2018) is used to parametrize endpoints of a finite line in the 3D space. Although this representation can be used to provide re-projection residuals of lines for camera pose optimization, it has the over-parameterization problems in landmark optimization. Similar to the *Euclidean*, a line at infinity can be represented as the *Plücker* coordinate via two three-dimensional vectors containing the direction of the line and normal based on the line and the camera coordinate frame as listed in Table 1. Furthermore, the dual quaternion approach (Kottas and Roumeliotis 2013) represents a line in 3D space using dual quaternions, which provides a concise way to represent rotations and translations in 3D space and can be used to encode the position and orientation of lines. The advantage of this approach is that it allows for easy composition of transformations, which makes it useful in applications such as robotics and animation. By multiplying the unit quaternion and the distance parameter, the *closest point* method (Yang and Huang 2019) can be considered as the

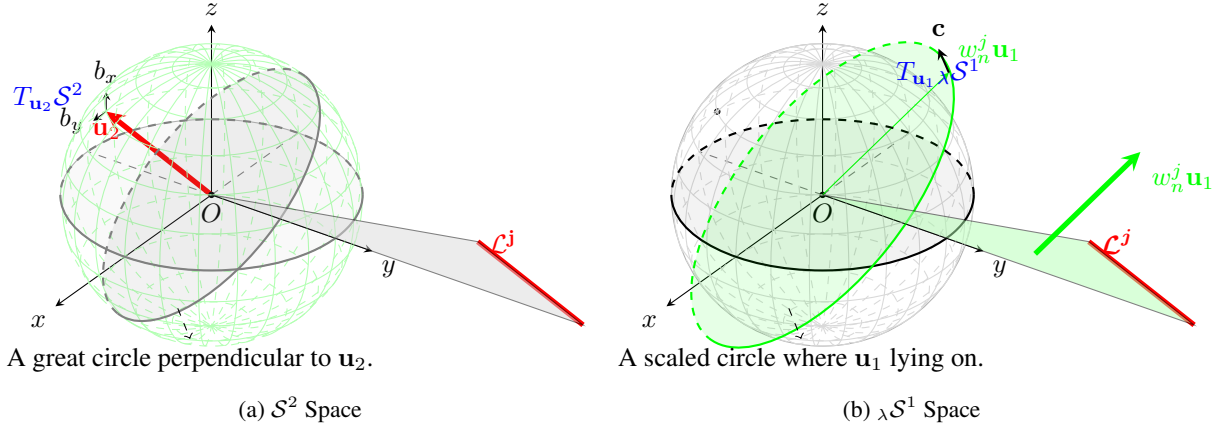


Figure 2: Illustration of the proposed parametrization for a line landmark \mathcal{L}^j . The vanishing direction vector \mathbf{u}_2 ($\|\mathbf{u}_2\| = 1$) and scaled normal vector $\omega_n^j \mathbf{u}_1$ ($\|\mathbf{u}_1\| = 1, \omega_n^j > 0$) are optimized on the tangent spaces $T_{\mathbf{u}_2}S^2$ of the sphere and $T_{\mathbf{u}_1}\lambda S^1$ of the scaled circle, respectively.

'closest point' for a 3D line. The transformation relationships between *Plücker*, *Quaternion* and *Closest Point* methods are listed in Table 1. The rotation matrix used in those representations can be optimized via *Lie algebras* which define the tangent spaces of related manifolds. For the *Spherical* form, a line can also be represented by three angles and a distance parameter. Instead of optimizing the orthogonal matrix through *Lie Groups* being special instances of the manifold, a more general Riemannian manifold is used to refine the vanishing and normal vectors subsequently in the proposed method.

Structure-SLAM (Li et al. 2020c) estimates the orientation using surface normals from monocular images, while Linear-SLAM (Joo et al. 2021) extracts planes from depth maps. Given a known rotation, the translation estimation becomes linear. The Manhattan World (MW) model assumes orthonormal landmarks and the Atlanta World (AW) model introduces multiple perpendicular horizontal directions. The multi-MW model (Yunus, Li, and Tombari 2021) enforces orthogonality within local regions instead of throughout the scene. However, such methods often neglect optimization within factor graphs. Recent approaches integrate structural constraints, lines and planes, directly into optimization. (Zhang et al. 2015) pioneered using parametric 3D lines as SLAM landmarks, enhancing traditional point-based methods. (Lu and Song 2015) extended this by incorporating diverse structural features within a multilayer feature graph (MFG) to improve environmental representation and pose estimation. Kimera-VIO (Rosinol et al. 2020) leverages 3D meshes to enforce coplanarity constraints within factor graphs. PLP-VIO (Li et al. 2020a) further refines this approach by incorporating line-based meshes to enhance spatial understanding. CoP (Li et al. 2020b) introduced a novel parameterization that represents points and lines using plane parameters to preserve geometric consistency during optimization. Beyond scene-specific models, Struct-VIO (Zhou et al. 2015; Zou et al. 2019) mitigates directional errors and reducing drift by parameterizing line segments parallel to

the local Manhattan world. Our method generalizes this by parameterizing all parallel lines, which uses the structural information to improve pose estimation accuracy in SLAM.

3 On-Manifold Representation of 3D Lines

3.1 Preliminary: Representation in Orthonormal

As shown in Table 1, a 3-dimensional finite line \mathbf{L}^w in the world coordinates can be represented by its two 3D endpoints, \mathbf{P}_s^w and \mathbf{P}_e^w , as $\mathbf{L}^w = [\mathbf{P}_s^w \ \mathbf{P}_e^w]$. For an infinite line, the direction and normal vectors can be used to represent the line $\mathcal{L}^w = [\mathbf{n}^w \ \mathbf{d}^w]$ based on the *Plücker* representation, where \mathbf{n}^w and \mathbf{d}^w can be derived from the endpoints \mathbf{P}_s^w and \mathbf{P}_e^w . This can be further expressed as the multiplication of several matrices via the following function:

$$\begin{aligned} \mathcal{L}^w &= [\mathbf{n}^w \ \mathbf{d}^w] \\ &= \begin{bmatrix} \frac{\mathbf{n}^w}{\|\mathbf{n}^w\|} & \frac{\mathbf{d}^w}{\|\mathbf{d}^w\|} \end{bmatrix} \begin{bmatrix} \|\mathbf{n}^w\| & 0 \\ 0 & \|\mathbf{d}^w\| \end{bmatrix}. \end{aligned} \quad (1)$$

We then use $\begin{bmatrix} \frac{\mathbf{n}^w}{\|\mathbf{n}^w\|} & \frac{\mathbf{d}^w}{\|\mathbf{d}^w\|} \end{bmatrix}$ and $\begin{bmatrix} \|\mathbf{n}^w\| & 0 \\ 0 & \|\mathbf{d}^w\| \end{bmatrix}$ to establish the following matrices:

$$\begin{cases} \mathbf{U} = \begin{bmatrix} \frac{\mathbf{n}^w}{\|\mathbf{n}^w\|} & \frac{\mathbf{d}^w}{\|\mathbf{d}^w\|} & \frac{\mathbf{n}^w \times \mathbf{d}^w}{\|\mathbf{n}^w \times \mathbf{d}^w\|} \end{bmatrix}; \\ \mathbf{W} = \begin{bmatrix} \|\mathbf{n}^w\|/\lambda & -\|\mathbf{d}^w\|/\lambda \\ \|\mathbf{d}^w\|/\lambda & \|\mathbf{n}^w\|/\lambda \end{bmatrix}. \end{cases} \quad (2)$$

Here, λ is represents $\sqrt{\|\mathbf{d}^w\|^2 + \|\mathbf{n}^w\|^2}$, $\mathbf{U} \in SO(3)$, and $\mathbf{W} \in SO(2)$.

In *quaternion-based* optimization methods (Yang and Huang 2019), \mathbf{U} is represented as a quaternion vector via $\bar{\mathbf{q}} = \mathcal{R}^{-1}(\mathbf{U})$, and the optimization process is implemented based on quaternion representation. With the widespread application of differentiable manifolds in SLAM optimization problems, the Orthonormal representation (Bartoli and Sturm 2005) maps the update process of $SO(3) \times SO(2)$ on the tangent space *Lie algebra* based on 4 degree-of-freedom

$[\boldsymbol{\rho}^T \ \omega]^T$ that is the minimal line representation widely used in Line-joined SLAM (Zuo et al. 2017; Li et al. 2020b) and VIO (He et al. 2018) systems.

3.2 Riemannian Representation of a Single 3D Line

We decouple the single line \mathcal{L}^j into two components: the unit direction vector \mathbf{u}_2 , and the scaled normal vector $\omega_n^j \mathbf{u}_1$. As illustrated in Figure 2, the direction vector \mathbf{u}_2 (with $\|\mathbf{u}_2\| = 1$) lies on the surface of the unit sphere \mathcal{S}^2 . The scaled normal vector $\omega_n^j \mathbf{u}_1$ lies on the plane ${}_\lambda \mathcal{S}^1$, which is centered at the origin and orthogonal to \mathbf{u}_2 .

Optimization on \mathcal{S}^2 . As illustrated in Figure 2a, the tangent space to \mathcal{S}^2 (at \mathbf{u}_2) is given by:

$$T_{\mathbf{u}_2} \mathcal{S}^2 \doteq \{\mathbf{x} : \|\mathbf{x}\| = 1, \mathbf{x} \in \mathbb{R}^3 | \mathbf{x}^T \mathbf{u}_2 = 0\}. \quad (3)$$

Here, $\mathbf{x}^T \mathbf{u}_2 = 0$ shows that the vectors \mathbf{x} in the tangent space are perpendicular to \mathbf{u}_2 . Although \mathcal{S}^2 is a non-linear 3D space, its tangent space $T_{\mathbf{u}_2} \mathcal{S}^2$ is a 2-DoF linear space. Based on the perpendicular bases \mathbf{b}_x and \mathbf{b}_y , any vector adjacent to \mathbf{u}_2 on the unit sphere can be represented.

In the representation process, $\delta\theta_1$ and $\delta\theta_2$, $[\delta\theta_1 \ \delta\theta_2]^T = \delta\boldsymbol{\theta}$, are corresponding disturbances towards \mathbf{b}_x and \mathbf{b}_y , respectively. Consequently, the perturbation $\delta\mathbf{m}$ on the tangent space can be represented as:

$$\delta\mathbf{m} = [\mathbf{b}_x \ \mathbf{b}_y] \begin{bmatrix} \delta\theta_1 \\ \delta\theta_2 \end{bmatrix}, \quad (4)$$

and the additive operation on the unit sphere is denoted as $\mathbf{u}_2 \boxplus \delta\mathbf{m}$, which maps $\delta\mathbf{m}$ backed to \mathcal{S}^2 via the *Riemannian exponential* $\text{Exp}_{\mathbf{u}_2}(\delta\mathbf{m})$, and the vector after perturbation is denoted as \mathbf{v}_2 computed via:

$$\begin{aligned} \mathbf{v}_2 &= \mathbf{u}_2 \boxplus \delta\mathbf{m} \\ &= \mathbf{u}_2 \cos \|\delta\mathbf{m}\| + \frac{\delta\mathbf{m}}{\|\delta\mathbf{m}\|} \sin \|\delta\mathbf{m}\|, \end{aligned} \quad (5)$$

where the perturbation $\delta\mathbf{m}$ is close to $\mathbf{0}$.

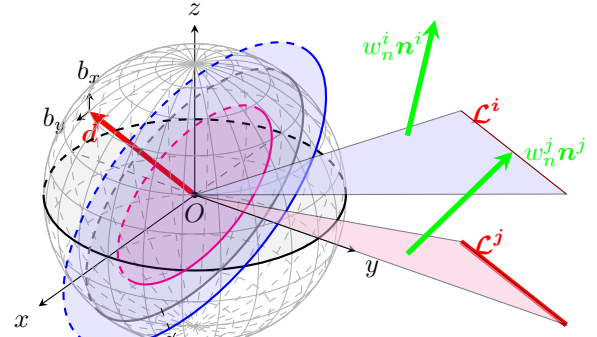
Optimization on ${}_\lambda \mathcal{S}^1$. Concurrently, the tangent space to ${}_\lambda \mathcal{S}^1$ is denoted as:

$$T_{\mathbf{u}_1} {}_\lambda \mathcal{S}^1 \doteq \{\mathbf{x} : \|\mathbf{x}\| = \lambda, \mathbf{x} \in \mathbb{R}^3 | \mathbf{x}^T \mathbf{u}_1 = \mathbf{x}^T \mathbf{u}_2 = 0\}. \quad (6)$$

Here, $\mathbf{x}^T \mathbf{u}_1 = \mathbf{x}^T \mathbf{u}_2 = 0$ shows that the vectors on the tangent space are perpendicular to \mathbf{u}_1 and \mathbf{u}_2 at the same time. Although ${}_\lambda \mathcal{S}^1$ is a non-linear 2D space, there is a base vector \mathbf{u}_3 which is orthogonal to both \mathbf{u}_1 and \mathbf{u}_2 . This base vector can be selected as \mathbf{u}_3 since $\mathbf{u}_3 = \mathbf{u}_2 \times \mathbf{u}_1$. With the perturbation of \mathbf{u}_2 , the tangent space of \mathbf{u}_1 is also perturbed by the orthogonal relationship. Based on the updated global direction \mathbf{v}_2 , we define the space $T_{\mathbf{u}_1} {}_\lambda \mathcal{S}^1$ based on $\mathbf{u}_3 = \mathbf{v}_2 \times \mathbf{u}_1$.

For a small angle $\delta\gamma$, we rotate \mathbf{u}_1 within the plane orthogonal to \mathbf{v}_2 by an angle $\delta\gamma$ to obtain the new vector \mathbf{v}_1 by using the base vector of the tangent space. Based on the Rodrigues rotation formula, the updated direction can be denoted as

$$\mathbf{v}_1 = \lambda \cdot (\cos(\delta\gamma) \mathbf{u}_1 + \sin(\delta\gamma) \mathbf{u}_3), \quad (7)$$



A great circle of the unit sphere.

Figure 3: Illustration of the parametrization for two parallel line landmarks \mathcal{L}^i and \mathcal{L}^j . The vanishing direction vector \mathbf{u}_2 and normalized normal vector \mathbf{u}_1 are optimized on the tangent spaces $T_{\mathbf{u}_2} \mathcal{S}^2$ of the sphere and $T_{\mathbf{u}_1} {}_\lambda \mathcal{S}^1$ of the circle, respectively.

which rotates \mathbf{u}_1 within the plane orthogonal to \mathbf{v}_2 by angle $\delta\gamma$. $\lambda \in \mathbb{R}_+$ is a scalar magnitude.

3.3 Unified Representation for Parallel Line Sets

As illustrated in Figure 3, our method naturally extends to a set of parallel lines by building upon the representation of a single 3D line. For a group of k parallel lines denoted as $\mathbb{S} = [\mathcal{L}_0^w, \mathcal{L}_1^w, \dots, \mathcal{L}_k^w]$, the shared vanishing direction is represented by a single unit vector \mathbf{u}_2 . Each line \mathcal{L}_i^w in the group is characterized by a local component \mathbf{u}_1^i and a scale ω^i . This results in a compact representation of the set as:

$$[\mathbf{u}_2, \omega^0 \mathbf{u}_1^0, \omega^1 \mathbf{u}_1^1, \dots, \omega^k \mathbf{u}_1^k], \quad (8)$$

where all $\omega^i \mathbf{u}_1^i$ lying on the circle ${}_{\omega^i} \mathcal{S}^1$ perpendicular to \mathbf{u}_2 . This leads to a minimal representation of the entire line group with $2 + 2k$ degrees of freedom: 2 DoF for the shared global direction \mathbf{u}_2 , and 2 DoF per line for its local component.

As shown in Figure 3, \mathbf{u}_2 lies on \mathcal{S}^2 and each \mathbf{u}_1^i lies on the associated circle orthogonal to \mathbf{u}_2 by the minimal representation on the unit sphere. Consequently, the minimal parameterization of the parallel line group follows the same format as the single-line case and can be written as:

$$[\delta\boldsymbol{\theta}, \delta\gamma^0, \dots, \delta\gamma^k, \lambda^0, \dots, \lambda^k], \quad (9)$$

where $\delta\boldsymbol{\theta}$ encodes the global direction \mathbf{u}_2 , $\delta\gamma^i$ represents the angular perturbation of \mathbf{u}_1^i on the circle, and λ^i denotes the perturbation corresponding distance scale. Since parallel lines \mathcal{L}^i and \mathcal{L}^j share the same direction vector \mathbf{u}_2 , the global vector \mathbf{u}_2 can thus be optimized via Equation 4 and 5. The associated local vectors $\omega^i \mathbf{u}_1^i$ and $\omega^j \mathbf{u}_1^j$ lie on the same plane defined by this tangent plane, therefore these local components can be optimized separately.

This unified formulation demonstrates the versatility of our approach that enables seamless extension from individual line landmarks to structurally consistent representations

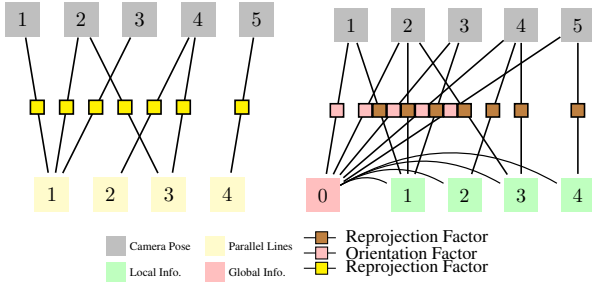


Figure 4: Factor graph representations for different line-based structures. Left: conventional line re-projection factors. Right: the proposed parallel line representation, explicitly separating global and local components with additional orientation and re-projection factors.

of parallel line groups within a common manifold-based optimization framework.

4 Optimization with Points and Lines

4.1 Graph Construction

The vertices in the point-line factor graphs \mathcal{G} include camera poses \mathcal{V}_{pose} , point landmarks \mathcal{V}_p , line landmarks \mathcal{V}_l and parallel-line sets \mathcal{V}_{para} . Specifically, camera pose $\mathbf{T}_{w,c_i} = \begin{bmatrix} \mathbf{R}_{w,c_i} & \mathbf{t}_{w,c_i} \\ \mathbf{0} & 1 \end{bmatrix}$, where $\mathbf{T}_{w,c_i} \in SE(3)$, $\mathbf{R}_{w,c_i} \in SO(3)$, and $\mathbf{t}_{w,c_i} \in \mathbb{R}^3$. Points used in the optimization module is parametrized as $\mathbf{P}_w^k = [x^k \ y^k \ z^k]^T$, and line landmarks are represented in minimal parameterization forms.

4.2 Factors and Constraints

Co-visibility connections (Mur-Artal, Montiel, and Tardos 2015; Mur-Artal and Tardós 2017; Campos et al. 2021) are built when two images detect the same landmark, such as a point or a line on the map. In this section, we define the co-visibility factors based on the re-projection models of point and line features.

Co-visibility factors from points. Based on the point feature measurement model, the measurement of the k^{th} global point landmark \mathbf{P}_w^k at frame c_j is represented as $\bar{\mathbf{p}}_k^j$ in the normalized coordinate, and the re-projection factor of a point feature is defined as $\mathbf{r}_p(\bar{\mathbf{p}}_k^j, \mathbf{P}_w^k, \mathbf{T}_{w,c_j})$.

Co-visibility factors from lines. Traditionally, the mapline \mathcal{L}_w^i in the world coordinate is transferred to the camera coordinates, and then re-projected on the image plane \mathbf{l}_k^j of viewpoint c_j . The error between the re-projected line \mathbf{l}_k^j and the two endpoints $\bar{\mathbf{p}}_{k,s}^j$ and $\bar{\mathbf{p}}_{k,e}^j$ of the extracted 2D line can be written as:

$$\mathbf{r}_l(\bar{\mathbf{p}}_{k,s}^j, \bar{\mathbf{p}}_{k,e}^j, \mathcal{L}_w^i, \mathbf{T}_{w,c_j}) = \begin{bmatrix} \text{dis}(\bar{\mathbf{p}}_{k,s}^j, \mathbf{l}_k^j) \\ \text{dis}(\bar{\mathbf{p}}_{k,e}^j, \mathbf{l}_k^j) \end{bmatrix}, \quad (10)$$

where $\text{dis}(\cdot)$ gives the distance between a point and a line.

Constraints between parallel lines. To enforce structural consistency, we incorporate additional constraints among groups of parallel lines. Specifically, for each mapline \mathcal{L}_w^i in a set of N parallel lines $\{\mathcal{L}_w^i\}_{i=1}^N$, its direction should be parallel to other lines in the set. The parallelism constraint is enforced by minimizing the angular deviation between the direction of each line \mathbf{u}_2^i . The residual is defined as:

$$\mathbf{r}_{\parallel}(\mathcal{L}_w^i, \{\mathcal{L}_w^j\}_{j=1, j \neq i}^N) = \frac{1}{N-1} \sum_{j=1, j \neq i}^N (1 - \mathbf{u}_2^{i\top} \mathbf{u}_2^j). \quad (11)$$

Here, the residual \mathbf{r}_{\parallel} encourages all lines in the group to remain parallel to the each other during optimization.

5 Experiments

We evaluate the proposed RiemanLine and StructRiemanLine parameterizations on both public benchmarks and simulated environments. Our goals are to assess: (i) pose estimation accuracy, (ii) landmark reconstruction quality, and (iii) the benefits of incorporating structural constraints within a unified Riemannian manifold representation.

Baselines. We compare against standard parameterizations widely used in SLAM and VO: **Euclidean XYZ** (Mur-Artal, Montiel, and Tardos 2015), **Orthonormal** (Bartoli and Sturm 2005), and **ImplicitLine** (Zhao et al. 2015). The Orthonormal form serves as the minimal representation for Closest Point (Yang and Huang 2019) and Quaternion (Kottas and Roumeliotis 2013) methods. All baselines are fed with the same co-visibility factor graph in each sequence.

Datasets. We use the ICL-NUIM benchmark (Handa et al. 2014) (eight indoor RGB-D sequences) and four TartanAir (Wang et al. 2020) sequences featuring photorealistic synthetic environments. Additionally, we evaluate on three challenging simulation sequences (corridor, box, sphere) generated using Open-Structure (Li et al. 2024).

Metrics. We report Absolute Trajectory Error (ATE) for camera localization, and angular errors (direction and normal) for line reconstruction. All results are averaged per sequence. Computations were performed on an Intel NUC Mini PC with Core i7-8700 CPU.

5.1 Evaluation on ICL-NUIM

Table 2 summarizes ATE RMSE and MEDIAN errors. The initial factor graphs show significant drift (e.g., RMSE 12.13 cm on *livingroom0*). The proposed **Point-StructRiemanLine** achieves the best overall accuracy across all eight sequences. By explicitly encoding parallel-line constraints into the minimal Riemannian representation, it reduces errors without introducing additional parameters. For example, *livingroom2* achieves RMSE 0.75 cm (MEDIAN 0.68 cm), and *office2* maintains RMSE 0.75 cm while preserving robust convergence behavior.

5.2 Evaluation on TartanAir

Table 3 reports ATE translation and rotation errors on the TartanAir benchmark. The proposed **StructRiemanLine**

Sequence	Initial		Optimization using Independent Primitives								Optimization using Structure Constraints			
	Factor Graph		Point		Point_OrthLine		Point_ImplicitLine		Point_RiemanLine		Point_OrthLine_Constr		Point_StructRiemanLine	
	RMSE	MEDIAN	RMSE	MEDIAN	RMSE	MEDIAN	RMSE	MEDIAN	RMSE	MEDIAN	RMSE	MEDIAN	RMSE	MEDIAN
livingroom0	12.13	1.95	1.14	0.69	0.81	0.38	0.96	0.40	0.81	0.38	0.81	0.38	0.81	0.37
livingroom1	2.15	1.57	1.67	1.24	4.13	4.22	0.92	0.81	1.19	0.71	3.58	3.60	0.90	0.55
livingroom2	12.95	6.95	1.61	0.80	0.79	0.71	1.18	0.90	0.78	0.71	0.79	0.72	0.75	0.68
livingroom3	18.26	13.93	11.64	11.43	6.70	6.33	6.67	6.76	6.71	6.34	6.71	6.34	6.65	6.33
office0	1.73	0.69	0.70	0.34	0.38	0.26	0.47	0.37	0.38	0.26	0.38	0.26	0.38	0.26
office1	11.93	5.48	7.68	5.22	1.81	0.89	9.78	7.81	1.89	0.87	1.81	0.87	1.76	0.73
office2	2.95	1.88	0.93	0.55	0.75	0.56	0.75	0.53	0.75	0.56	0.76	0.56	0.75	0.56
office3	7.56	2.47	1.22	0.66	0.78	0.49	1.86	0.77	0.79	0.51	0.85	0.53	0.77	0.46

Table 2: Comparison of translation (APE) RMSE (cm) and MEDIAN (cm) on the ICL-NUIM (Handa et al. 2014) benchmark dataset. The best results are highlighted in **bold**.

Table 3: Comparison of APE RMSE (translation (cm) and rotation (degree) on the TartanAir dataset.

Sequence	Carwelding		Hospital		Office		JapaneseAlley	
	Trans.	Rot.	Trans.	Rot.	Trans.	Rot.	Trans.	Rot.
Initial	14.74	10.89	33.78	26.83	57.00	47.78	10.92	5.23
Point_OrthLine	4.47	0.16	5.32	4.83	43.25	29.23	3.75	2.80
Point_OrthLine_Constr	4.56	0.16	5.49	4.97	50.04	39.50	3.68	2.72
Point_RiemanLine	4.46	0.16	7.29	6.60	40.95	26.70	3.85	2.92
Point_StructRiemanLine	4.08	0.15	2.91	2.04	15.60	12.08	3.65	2.68

Table 4: Comparison of line reconstruction (direction and normal) performance MEDIAN (degree) on the TartanAir dataset.

Sequence	Carwelding		Hospital		Office		JapaneseAlley	
	direc.	normal	direc.	normal	direc.	normal	direc.	normal
Point_OrthLine	1.52	1.42	5.16	4.11	3.89	4.49	0.88	0.86
Point_OrthLine_Constr	0.92	0.93	5.05	2.54	2.04	2.28	0.46	0.42
Point_RiemanLine	1.55	1.43	5.38	4.68	3.89	4.48	0.88	0.73
Point_StructRiemanLine	0.82	0.83	1.60	0.91	0.04	0.51	0.07	0.15

achieves the most significant improvement in structurally rich indoor sequences. On *Hospital*, the translation RMSE drops from 33.78 cm (Initial) and 7.29 cm (**RiemanLine**) to only 2.91 cm, while the rotation RMSE decreases from 26.83° to 2.04° . Similarly, on *Office*, the translation error is reduced by over **40%** compared to Point-OrthLine and Point-RiemanLine, demonstrating that the proposed parallel-line manifold representation provides strong orientation priors that are especially beneficial in man-made environments with dominant structural regularities. These results validate that explicitly encoding shared vanishing directions within the factor graph not only improves translational accuracy but also significantly enhances rotational consistency, a critical factor for large indoor scene reconstruction.

Line reconstruction. Table 4 reports median angular errors. StructRiemanLine achieves the lowest direction and normal errors across all TartanAir sequences. In *Hospital*, the direction error is reduced to 1.60° and the normal error to 0.91° , validating that structural encoding improves both pose estimation and landmark quality. Figure 5 shows the cumulative distribution of angular errors for line direction and normal estimation on the *Hospital* sequence. The proposed StructRiemanLine achieves the steepest rise and highest saturation, indicating that over 90% of reconstructed lines fall within 2° of the ground truth for both direction and normal vectors. Compared to Point-Orthonormal and Point-RiemanLine, which exhibit heavier tails beyond 5° , StructRiemanLine demonstrates significantly reduced variance.

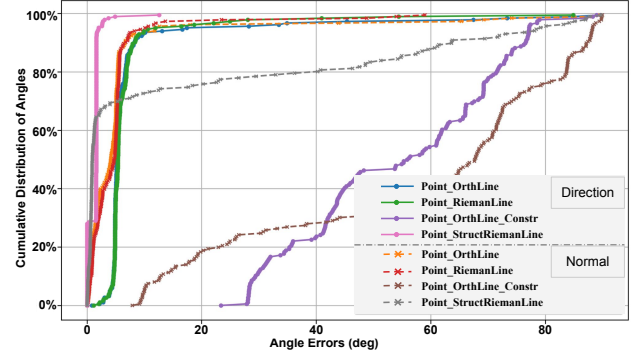


Figure 5: Line reconstruction errors of different methods in the *Hospital* sequence.

This confirms that encoding parallelism within the Riemanian manifold not only lowers median error (Table 4) but also improves the overall consistency of structural line reconstruction.

5.3 Simulations

Figure 7 illustrates the synthetic environments that are *corridor*, *box*, and *sphere*. In the corridor scenario, a rectangular arrangement of green points forms a corridor-like structure with blue structural lines embedded within, while a red trajectory traces a loop along the corridor’s center. The box scenario shows a compact cluster of green points representing a box-shaped space, intersected by blue line segments, with a red trajectory following a wave-like path through the volume. The sphere scenario depicts a roughly spherical distribution of green points surrounded by blue structural lines, where the red trajectory forms a dense circular pattern around the sphere’s surface.

Table 5 reports ATE RMSE. While both RiemanLine and Orthonormal perform similarly on simple structures, StructRiemanLine consistently achieves the lowest translation and rotation errors. In the *sphere* scenario, it reduces translation RMSE to 1.16 cm and maintains minimal orientation drift, confirming the benefits of enforcing parallelism constraints in structurally symmetric environments.

Figure 6 further compares pitch and roll estimation errors in the *sphere* simulation. Point-Orthonormal and Point-RiemanLine exhibit small but noticeable oscillations, while StructRiemanLine maintains the closest alignment with

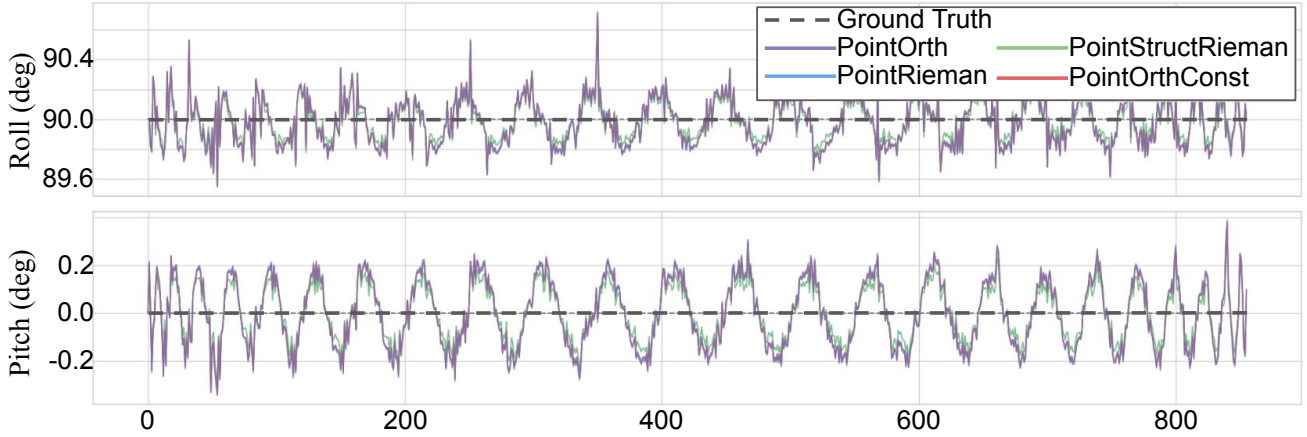


Figure 6: Pitch and roll angle errors for the sphere sequence in the simulation dataset. The plots compare the estimated orientations of different methods against the ground truth.

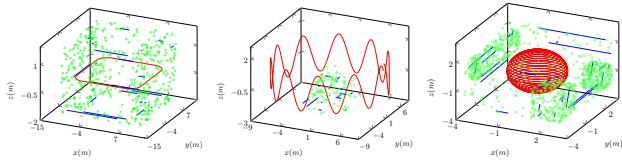


Figure 7: Visualization of the simulation scenarios: *corridor*, *box*, and *sphere*. Points, lines, and trajectories are shown in green, blue, and red, respectively.

Table 5: Comparison of translation (APE RMSE (cm)) and rotation (APE RMSE (degree)) on the simulation dataset.

Method	corridor		box		sphere	
	Trans.	Rot.	Trans.	Rot.	Trans.	Rot.
Initial	10.57	1.54	9.67	0.85	25.99	5.49
Point_OrthLine	4.24	0.32	2.09	0.23	1.19	0.19
Point_OrthLine_Constr	4.29	0.32	2.09	0.23	1.19	0.19
Point_RiemanLine	4.24	0.32	2.09	0.23	1.20	0.19
Point_StructRiemanLine	4.02	0.31	2.08	0.23	1.16	0.19

ground truth across the trajectory.

The variance remains below 0.2° throughout, demonstrating that enforcing parallelism constraints on the Riemannian manifold enhances not only translational accuracy (Table 5) but also rotational stability. This is particularly critical in symmetric environments where orientation drift often accumulates in conventional line-based SLAM systems.

Runtime and Complexity Analysis. Table 6 reports the parameter complexity and solver runtime on the *box* simulation sequence, which contains 447 camera poses, 130 point landmarks, 20 line landmarks, and 2 parallel-line groups. Landmarks observed by fewer than three cameras are pruned prior to optimization to ensure a consistent and well-constrained factor graph. Starting from the *Point-only* baseline, the inclusion of 20 line landmarks in **Point-OrthLine-Constr** introduces 20 additional parameter blocks and **80** new parameters due to the conventional $4n$

Metric	Para. Blocks	Effi Paras.	Resi. Blocks	Resi.	Time (s)
<i>Point</i>	577	3072	36010	37010	53.90
Point_OrthLine_Constr	597	3152	41773	83452	97.62
Point_StructRiemanLine	579	3116	41679	83358	49.62

Table 6: Comparison of parameter complexity and total solver runtime between the conventional Orthonormal representation with additional parallelism constraints and the proposed minimal parametrization on the *box* sequence

minimal parameterization. In contrast, the proposed **StructRiemanLine** requires only **44** parameters to represent the same 20 lines, as 19 of them are encoded within two parallel-line groups and a single independent line under the compact $2n + 2$ formulation.

In terms of computational efficiency, the total optimization time drops from **97.62 s** to **49.62 s**, yielding an approximate 49% overall speed-up. This improvement is consistent with the reduction in parameter blocks ($597 \rightarrow 579$) and state dimensionality ($3152 \rightarrow 3116$), which together produce a sparser and better-conditioned Hessian.

6 Conclusion and Future Works

We have presented a novel minimal representation for 3D line landmarks. Unlike conventional approaches, the proposed parameterization not only encodes individual lines with minimal degrees of freedom, but also naturally accommodates structural regularities such as sets of parallel lines. Building upon this representation, we introduced a joint factor graph framework that integrates both co-visibility and structural factors, enabling more accurate and efficient optimization of camera poses and landmarks compared to traditional point-line co-visibility graphs.

Looking ahead, we envision incorporating the proposed parameterization into full SLAM and visual odometry pipelines to achieve more robust tracking and high-fidelity reconstruction in large-scale environments. A particularly promising direction is the development of an *orientation clo-*

Scene	Num. of Points	Num. of Lines	Num. of Pose
livingroom0	1384	69	1508
livingroom1	1599	96	965
livingroom2	2118	130	880
livingroom3	1063	97	1240
office0	3405	73	1507
office1	2026	70	965
office2	2446	67	880
office3	2402	128	1240
Carwelding	2484	196	357
Hospital	1385	186	563
JapaneseAlley	1295	146	510
Office	3293	130	612

Table 7: Statistics of the initial factor graphs constructed for the ICL-NUIM and TartanAir datasets. The table reports the number of reconstructed 3D points, line landmarks, and camera poses for each sequence, covering a range of indoor synthetic environments (livingroom0–3, office0–3) and photorealistic scenes (Carwelding, Hospital, JapaneseAlley, Office). These statistics reflect the structural diversity and varying scales of the evaluated datasets.

sure module that leverages the shared vanishing directions of parallel lines within the factor graph to mitigate drift.

A Experiment Setup and Input Data

We provide additional details about our experimental setup, input graph construction, and evaluation protocol. Note that the datasets used are public benchmarks and not contributions of this work. Our focus is on demonstrating how the same input factor graphs are used across all optimization methods to ensure a fair and controlled comparison.

A.1 Initial Factor Graphs

Figure 9 illustrates the initial factor graphs generated using the SLAM baseline (Li et al. 2024) across sequences from the ICL-NUIM and TartanAir datasets. Green points and lines represent reconstructed 3D landmarks, while red curves denote camera trajectories. The ICL-NUIM dataset contains indoor environments (livingroom, office), and TartanAir provides photorealistic scenes (Carwelding, Hospital, etc.), introducing diverse structural layouts.

Table 7 summarizes the scale of the optimization problems, reporting the number of points, lines, and poses per sequence. Among the ICL-NUIM indoor scenes, office0 contains the largest number of points (3405) and poses (1507), while office2 and office1 have fewer line features (67 and 70), indicating limited structural edges. In contrast, the TartanAir scenes such as Carwelding and Hospital exhibit significantly more line landmarks (196 and 186), reflecting the prevalence of strong man-made structures. These statistics highlight the varying geometric complexity and structural diversity present in different scenes.

A.2 Observation Relationships

To construct the factor graph, we associate camera poses with the 3D landmarks they observe. Figure 8 visualizes these relationships in the *office0* sequence using color-coded

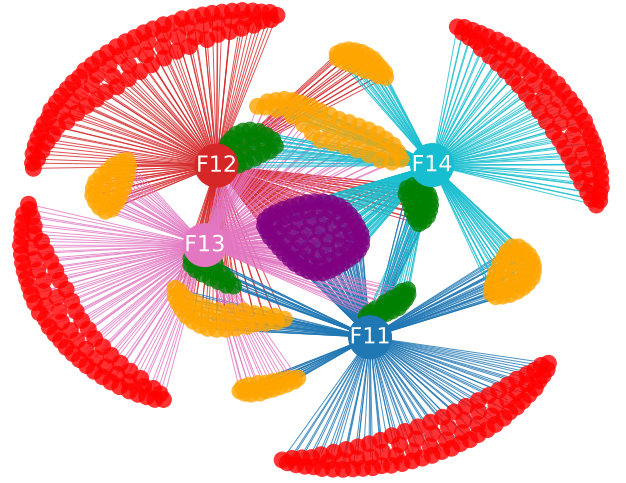


Figure 8: Visualization of observation relationships in the *office0* scene. For clarity, we only display 3D landmarks observed by four selected frames (F11–F14). Each line connects a frame to its observed landmarks. The color of each landmark encodes its observation frequency among the four frames: red indicates observation by one frame, yellow by two, green by three, and purple by all four. This visualization highlights the redundancy and overlap in landmark-frame associations used to construct the factor graph.

frequency of observations across four frames (F11–F14), highlighting how the observation relationship is embedded in the graph structure.

B Optimization Setup and Factor Definitions

To ensure a fair comparison of different optimization methods, we **separate the perception and optimization stages**. After clearly introducing the inputs generated by the SLAM baseline (Li et al. 2024), we further provide the implementation details of these optimization algorithms.

B.1 Cost Function Components

Co-visibility connections ((Mur-Artal, Montiel, and Tardos 2015; Mur-Artal and Tardós 2017; Campos et al. 2021)) are built when two images detect the same landmark, such as a point or a line in the map. Based on the re-projection models of point and line features, the co-visibility factors are defined in this section.

Table 8 provides an overview of the loss functions used by the methods under comparison. Our proposed StructRiemannLine uses a Riemannian manifold-based representation to jointly optimize camera poses and minimal line parameters, encoding parallel structure implicitly. This contrasts with prior methods like OrthLine-Constr, which require explicit constraint terms to enforce parallelism. Our method achieves lower dimensionality and better convergence properties while maintaining structural consistency.

Table 8 summarizes the loss functions employed by different factor graph optimization methods. Each method op-

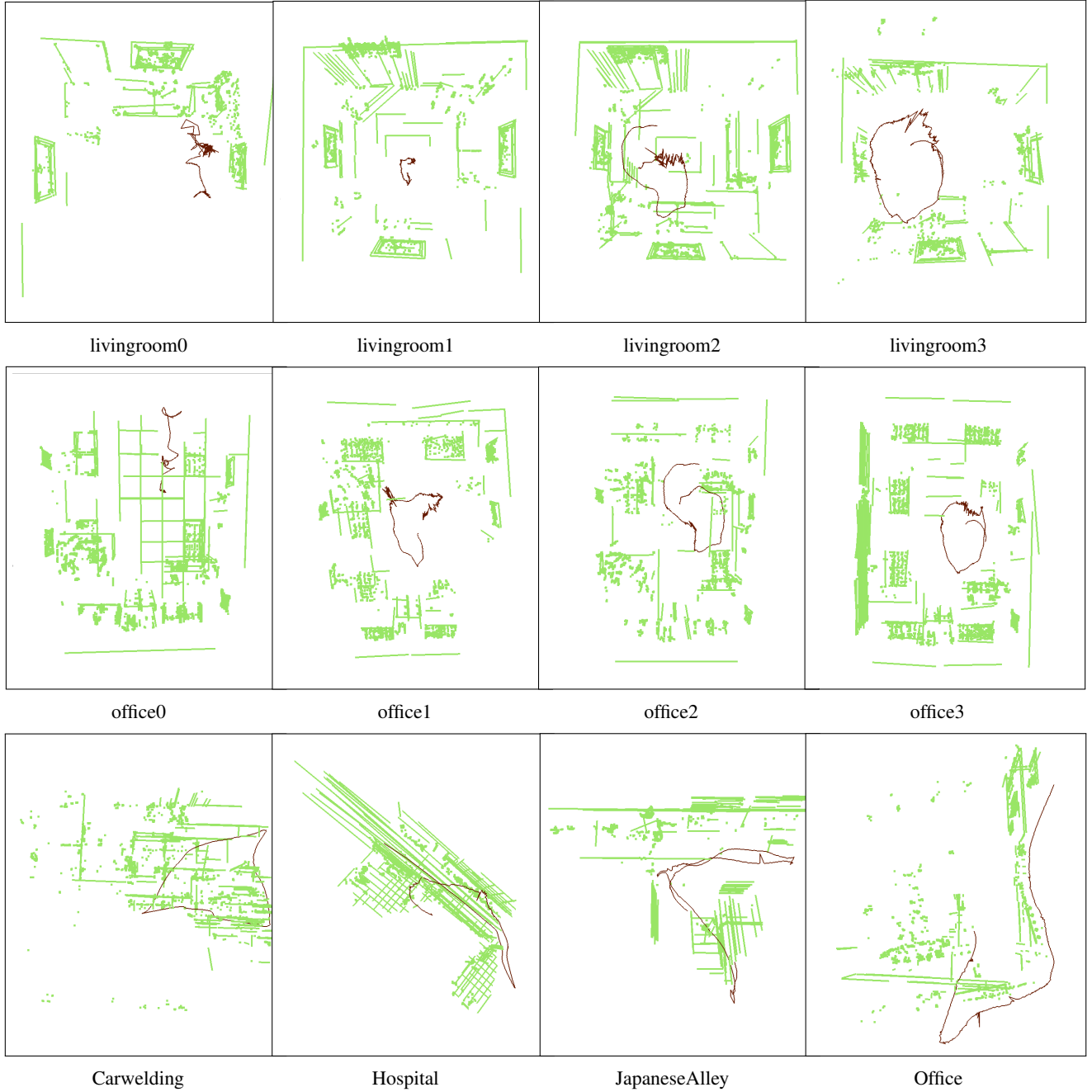


Figure 9: Visualization of the initial factor graphs generated by the SLAM baseline (Li et al. 2024) of the ICL-NUIM and TartanAir datasets. Each subfigure illustrates the reconstructed scene structure with point and line landmarks shown in green and camera trajectories overlaid in red. The first two rows correspond to the ICL-NUIM livingroom and office sequences, while the last row depicts TartanAir scenes including Carwelding, Hospital, JapaneseAlley, and Office. These visualizations highlight the diversity of geometric structures across synthetic indoor environments and photorealistic outdoor scenes, serving as the starting point for subsequent optimization.

Method	Loss Function
Point	$\min_{\mathcal{X}} \sum_{(i,j) \in \mathcal{E}_p} \rho(\ \mathbf{r}_p\ ^2)$
Point_OrthLine	$\min_{\mathcal{X}} \sum_{(i,j) \in \mathcal{E}_p} \rho(\ \mathbf{r}_p\ ^2) + \sum_{(i,j) \in \mathcal{E}_l} \rho(\ \mathbf{r}_l\ ^2)$
Point_OrthLine_Constr	$\min_{\mathcal{X}} \sum_{(i,j) \in \mathcal{E}_p} \rho(\ \mathbf{r}_p\ ^2) + \sum_{(i,j) \in \mathcal{E}_l} \rho(\ \mathbf{r}_l\ ^2) + \sum_{(i,j) \in \mathcal{E}_{ }} \rho(\ \mathbf{r}_{ }\ ^2)$
Point_RiemanLine	$\min_{\mathcal{X}} \sum_{(i,j) \in \mathcal{E}_p} \rho(\ \mathbf{r}_p\ ^2) + \sum_{(i,j) \in \mathcal{E}_l} \rho(\ \mathbf{r}_l\ ^2)$
Point_StructRiemanLine	$\min_{\mathcal{X}} \sum_{(i,j) \in \mathcal{E}_p} \rho(\ \mathbf{r}_p\ ^2) + \sum_{(i,j) \in \mathcal{E}_l} \rho(\ \mathbf{r}_l\ ^2)$

Table 8: Loss functions for different factor graph optimization methods. All these parameters are introduced in Section B.1.

timizes a total cost comprising different residual terms:

- \mathbf{r}_p : point reprojection residual, measuring the distance between the observed and projected 2D points;
- \mathbf{r}_l : line reprojection residual, quantifying the alignment between observed 2D line segments and the projection of 3D lines;
- $\mathbf{r}_{||}$: parallelism constraint residual, enforcing geometric structure by minimizing the angular deviation between grouped lines.

The baseline **Point** method considers only point reprojection. **Point-OrthLine** adds line-based factors using the orthonormal line representation. **Point-OrthLine-Constr** explicitly introduces additional parallelism constraints between lines via $\mathbf{r}_{||}$. In contrast, both **Point-RiemanLine** and **Point-StructRiemanLine** naturally encode line directions and structural regularity using the proposed Riemannian manifold representation, eliminating the need for explicit $\mathbf{r}_{||}$ constraints. This unified and minimal formulation improves convergence stability while preserving geometric consistency.

The complete objective can be written in general form as:

$$\min_{\mathcal{X}} \sum_{(i,j) \in \mathcal{E}_p} \rho(\|\mathbf{r}_p\|^2) + \sum_{(i,j) \in \mathcal{E}_l} \rho(\|\mathbf{r}_l\|^2) + \sum_{(i,j) \in \mathcal{E}_{||}} \rho(\|\mathbf{r}_{||}\|^2), \quad (12)$$

where $\rho(\cdot)$ denotes the robust Cauchy loss function, and \mathcal{X} contains all camera poses and 3D landmark parameters.

B.2 Detailed Residuals

Co-visibility Factors from Points. Given the i^{th} global 3D point landmark $\mathbf{P}_i = [x_i, y_i, z_i]^T$ and its observation in frame c_j , the 2D measurement is denoted as $\bar{\mathbf{p}}_i^j = [u_i^j, v_i^j, 1]^T$ in normalized coordinates. The point reprojection residual is defined as:

$$\mathbf{r}_p(\mathbf{p}_i^j, \mathbf{P}_i, \mathcal{X}) = \mathbf{K} \overline{\mathbf{R}_{w,j}^T (\mathbf{P}_i - \mathbf{t}_{w,j})} - \bar{\mathbf{p}}_i^j, \quad (13)$$

where \mathbf{K} is the intrinsic calibration matrix, and $\overline{(\cdot)}$ denotes the normalization to image plane coordinates.

Co-visibility Factors from Line Features. We adopt the Plücker line representation. A 3D line \mathcal{L}^w in world coordinates is transformed to the i^{th} camera frame using:

$$\mathcal{L}^i = \begin{bmatrix} \mathbf{n}^i \\ \mathbf{d}^i \end{bmatrix} = \mathcal{T}_{c_i,w} \begin{bmatrix} \mathbf{n}^w \\ \mathbf{d}^w \end{bmatrix}, \quad (14)$$

where $\mathcal{T}_{c_i,w} = \begin{bmatrix} \mathbf{R}_{c_i,w} & [\mathbf{t}_{c_i,w}]_{\times} \mathbf{R}_{c_i,w} \\ \mathbf{0} & \mathbf{R}_{c_i,w} \end{bmatrix}$, and $[\cdot]_{\times}$ denotes the skew-symmetric matrix.

In the image plane, the two endpoints of the projected 3D line, \mathbf{P}_s and \mathbf{P}_e , are transformed to:

$$\bar{\mathbf{p}}_k = \mathbf{K} \bar{\mathbf{P}}_k, \quad k \in \{s, e\}, \quad (15)$$

where $\bar{\mathbf{P}}_k$ is the normalized 3D point in the camera frame. The projected 2D line \mathcal{L}^j is computed as:

$$\mathcal{L}^j = \bar{\mathbf{p}}_s \times \bar{\mathbf{p}}_e = \mathcal{K}(\bar{\mathbf{P}}_s \times \bar{\mathbf{P}}_e) = \mathcal{K} \mathbf{n}^j, \quad (16)$$

where the matrix \mathcal{K} is given by:

$$\mathcal{K} = \begin{bmatrix} f_y & 0 & 0 \\ 0 & f_x & 0 \\ -f_y c_x & -f_x c_y & f_x f_y \end{bmatrix}. \quad (17)$$

Given the detected 2D line segment in the image, with endpoints \mathbf{p}_s^j and \mathbf{p}_e^j , the residual between this observation and the projected line is:

$$\mathbf{r}_l(\mathbf{p}_{k,s}^j, \mathbf{p}_{k,e}^j, \mathcal{L}^w, \mathcal{X}) = \begin{bmatrix} \text{dis}(\mathbf{p}_{k,s}^j, \mathcal{L}^j) \\ \text{dis}(\mathbf{p}_{k,e}^j, \mathcal{L}^j) \end{bmatrix}, \quad (18)$$

where the point-to-line distance is defined as:

$$\text{dis}(\mathbf{p}, \mathcal{L}) = \frac{\mathbf{p}^T \cdot \mathbf{l}}{\sqrt{l_1^2 + l_2^2}}. \quad (19)$$

Here, $\mathcal{L}^j = [l_0, l_1, l_2]^T$ is the homogeneous representation of the 2D line, and $\mathbf{p} = [\bar{x}, \bar{y}, 1]^T$ is the normalized endpoint coordinate.

B.3 Jacobians of StructRiemanLine

The proposed Riemannian parameterization for line landmarks is defined as $\mathcal{R} = [\delta\theta \ \delta\gamma \ s]$, where $\delta\theta$ is a 2D tangent vector on the sphere \mathbb{S}^2 for the global direction, and $(\delta\gamma, s)$ encode the local line component. Based on the line residual \mathbf{r}_l , the Jacobian with respect to the parameters is computed as:

$$\frac{\partial \mathbf{r}_l}{\partial \mathcal{R}} = \begin{bmatrix} \frac{\partial \mathbf{r}_l}{\partial \mathcal{L}^w} \frac{\partial \mathcal{L}^w}{\partial \delta\theta} & \frac{\partial \mathbf{r}_l}{\partial \mathcal{L}^w} \frac{\partial \mathcal{L}^w}{\partial \delta\gamma} & \frac{\partial \mathbf{r}_l}{\partial \mathcal{L}^w} \frac{\partial \mathcal{L}^w}{\partial s} \end{bmatrix}. \quad (20)$$

We denote the three blocks of the Jacobian as \mathbf{J}_{θ}^l , \mathbf{J}_{γ}^l , and \mathbf{J}_s^l , respectively.

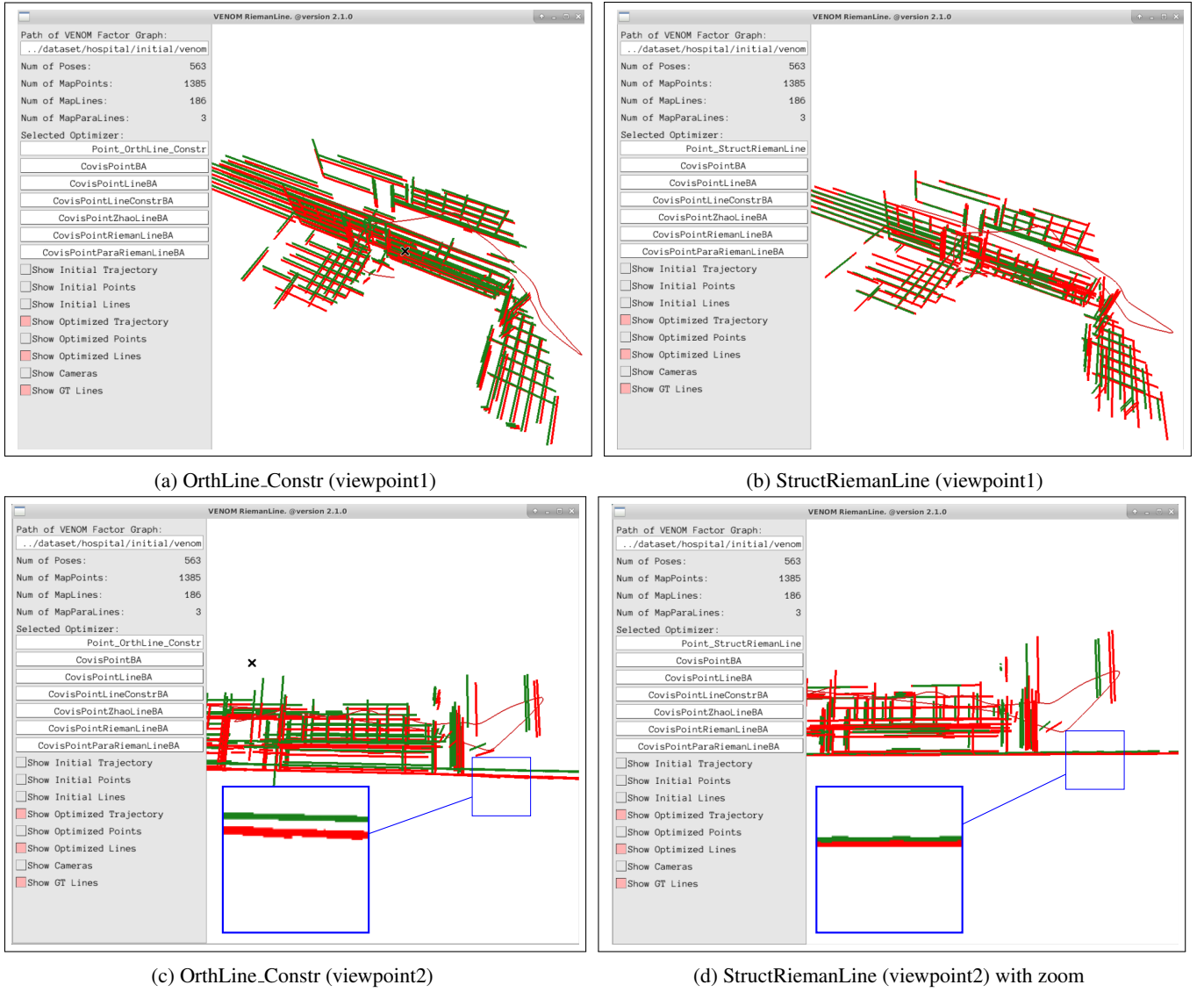


Figure 10: Line reconstruction comparison and software interface visualization on the *Hospital* sequence.

Since the world-frame Plücker line is represented as $\mathcal{L}^w = [s\mathbf{u}_1^T \ \mathbf{u}_2^T]^T$, the total Jacobian is derived through the chain rule:

$$\frac{\partial \mathbf{r}_l}{\partial \mathcal{L}^w} = \frac{\partial \mathbf{r}_l}{\partial \mathbf{l}} \frac{\partial \mathbf{l}}{\partial \mathcal{L}^c} \frac{\partial \mathcal{L}^c}{\partial \mathcal{L}^w}, \quad (21)$$

where $\frac{\partial \mathbf{l}}{\partial \mathcal{L}^c} = [\mathcal{K} \ \mathbf{0}]$, and the transformation from world to camera coordinates is given by:

$$\frac{\partial \mathcal{L}^c}{\partial \mathcal{L}^w} = \mathcal{T}_{c_i, w} = \begin{bmatrix} \mathbf{R}_{c_i, w} & [\mathbf{t}_{c_i, w}]_{\times} \mathbf{R}_{c_i, w} \\ \mathbf{0} & \mathbf{R}_{c_i, w} \end{bmatrix}. \quad (22)$$

Global Component Jacobian. The global direction $\mathbf{u}_2 \in \mathbb{S}^2$ is updated on the tangent space via the local perturbation $\delta\theta$. Using the exponential map, the updated direction vector becomes:

$$\mathbf{v}_2 = \cos(\delta)\mathbf{u}_2 + \sin(\delta)\dot{\delta\mathbf{m}}, \quad (23)$$

where $\delta = \|\delta\mathbf{m}\|$, $\dot{\delta\mathbf{m}} = \frac{\delta\mathbf{m}}{\delta}$, and $\delta\mathbf{m} = \mathbf{B}\delta\theta$ with \mathbf{B} being the tangent basis at \mathbf{u}_2 .

The Jacobian with respect to $\delta\theta$ is computed via:

$$\begin{aligned} \frac{\partial \mathbf{v}_2}{\partial \delta\mathbf{m}} &= -\sin(\delta)\mathbf{u}_2 \cdot \frac{\partial \delta}{\partial \delta\mathbf{m}} + \cos(\delta) \frac{\partial \delta}{\partial \delta\mathbf{m}} \dot{\delta\mathbf{m}} + \sin(\delta) \frac{\partial \dot{\delta\mathbf{m}}}{\partial \delta\mathbf{m}}, \\ \frac{\partial \delta}{\partial \delta\mathbf{m}} &= \dot{\delta\mathbf{m}}^T, \quad \frac{\partial \dot{\delta\mathbf{m}}}{\partial \delta\mathbf{m}} = \frac{1}{\delta} (\mathbf{I} - \delta\dot{\delta\mathbf{m}}\dot{\delta\mathbf{m}}^T), \end{aligned} \quad (24)$$

and the total Jacobian with respect to $\delta\theta$ is given by:

$$\frac{\partial \mathbf{v}_2}{\partial \delta\theta} = \frac{\partial \mathbf{v}_2}{\partial \delta\mathbf{m}} \cdot \mathbf{B}. \quad (25)$$

Local Component Jacobians. The local component \mathbf{v}_1 is expressed as a rotated version of \mathbf{u}_1 by an in-plane rotation

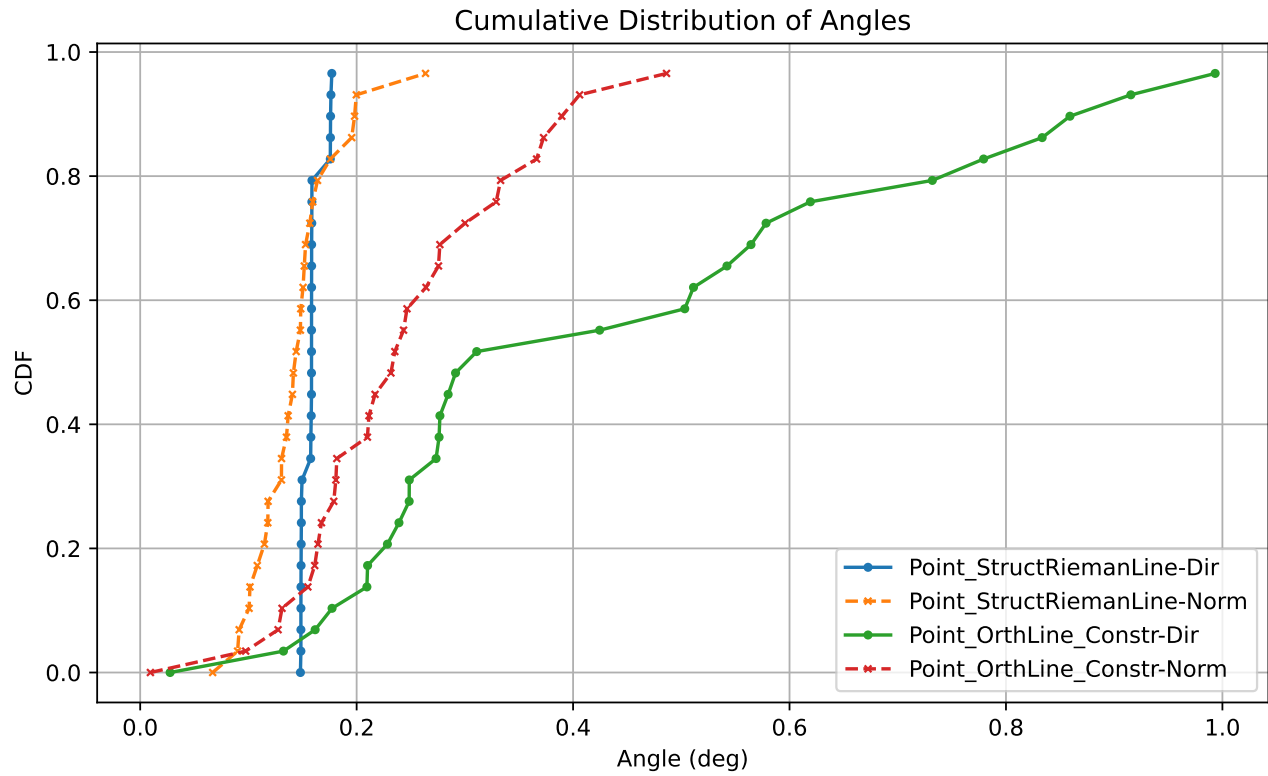
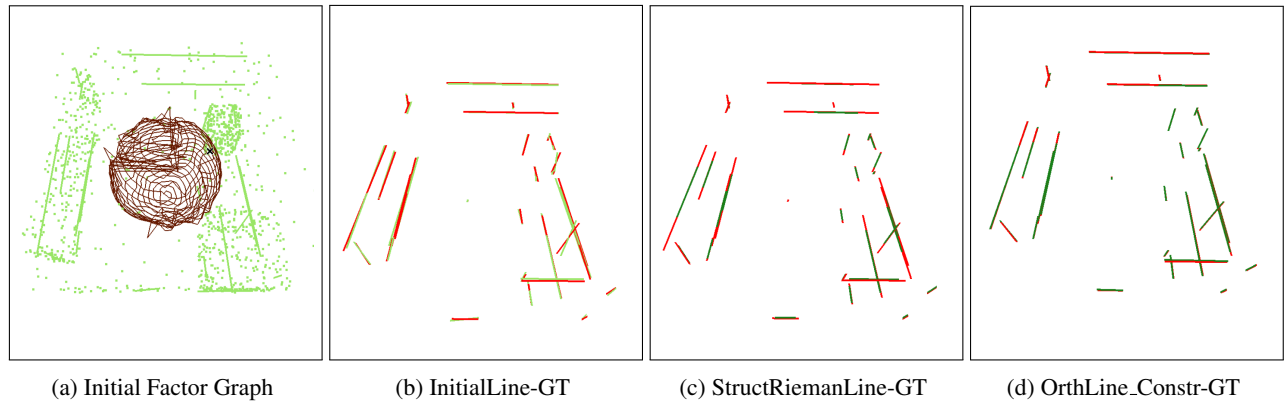


Figure 11: Comparison of line reconstruction in the Sphere sequence. (a) Initial factor graph with raw points and lines; (b) Reconstructed lines from the initial factor graph aligned with the ground truth (GT); (c) Results using the proposed StructRiemanLine method with structural constraints; (d) Results using the baseline OrthLine method. The bottom plot shows the Cumulative Distribution Function (CDF) of angular deviations between estimated and ground-truth lines for direction (-Dir) and normal vector (-Norm) components.

angle $\delta\gamma$ and magnitude s . The Jacobians are:

$$\begin{cases} \frac{\partial \mathbf{v}_1}{\partial s} = \cos(\delta\gamma)\mathbf{u}_1 + \sin(\delta\gamma)\mathbf{u}, \\ \frac{\partial \mathbf{v}_1}{\partial \delta\gamma} = s \cdot (-\sin(\delta\gamma)\mathbf{u}_1 + \cos(\delta\gamma)\mathbf{u}). \end{cases} \quad (26)$$

These derivatives are used to construct the full Jacobian of the residual \mathbf{r}_l with respect to the Riemannian line representation \mathcal{R} during optimization.

C Line Reconstruction Quality Analysis

To comprehensively evaluate the reconstruction quality of different methods, we present qualitative and quantitative comparisons across two representative scenes: Hospital (Figure 10) and Sphere (Figure 11). These comparisons reveal the structural correctness of line-based reconstruction.

Figure 10 shows side-by-side reconstructions and software interface visualizations from two viewpoints. In particular: (a, c) depict results from the baseline OrthLine-Constr, which often suffers from layering artifacts: structurally connected lines appear misaligned across depth layers, disrupting planar coherence. (b, d) show our proposed StructRiemmanLine, which maintains strong directional consistency and structural integrity across the scene.

To highlight this, we use zoomed-in spy boxes in sub-figures (c, d) that focus on a problematic region. The baseline method clearly exhibits vertical stratification, while our method preserves the planar alignment, verifying the benefit of our structure-aware Riemannian representation.

To further validate the reconstruction accuracy, we benchmark against ground truth line segments in synthetic scenes.

CDF Analysis on the Sphere sequence. The cumulative distribution function (CDF) plots at the bottom of Figures 11 visualize the angular errors: Direction error (-Dir) and normal error (-Norm) are evaluated between predicted and GT lines.

Our method achieves over 80% of lines within 0.2° angular error, significantly outperforming the baseline whose curves decay more slowly, indicating larger variance and wider error spread.

This confirms that our minimal, structure-aware line representation is both numerically stable and geometrically accurate, especially in challenging environments with dominant structural priors.

To further evaluate the geometric accuracy of the reconstructed 3D lines, we compare the angular errors between the predicted line parameters and the ground-truth lines on the *Sphere* dataset, which provides accurate annotations of line directions and normal vectors.

Table 9 reports the mean, median, standard deviation, and RMSE of angular errors (in degrees) for both the direction and normal vectors. Our proposed method, **StructRiemmanLine**, consistently outperforms the baseline **OrthLine-Constr** in all metrics. Specifically, StructRiemmanLine achieves a mean direction error of 0.158° and a normal error of 0.143° , substantially lower than the 0.429° and 0.240° errors from OrthLine-Constr, respectively. The

Dataset	Method / Metric	Mean	Median	Std	RMSE
Sphere	StructRiemmanLine - Direction	0.158	0.158	0.009	0.158
	StructRiemmanLine - Normal	0.143	0.142	0.039	0.148
	OrthLine_Constr - Direction	0.429	0.291	0.260	0.502
	OrthLine_Constr - Normal	0.240	0.232	0.102	0.261

Table 9: Comparison of angular errors (in degrees) for Direction and Normal vectors on the sphere sequence. Mean, median, std, and RMSE are reported.

standard deviation and RMSE also indicate more stable and accurate estimation with our method.

References

- Bartoli, A.; and Sturm, P. 2005. Structure-from-motion using lines: Representation, triangulation, and bundle adjustment. *Computer vision and image understanding*, 100(3): 416–441.
- Campos, C.; Elvira, R.; Rodríguez, J. J. G.; Montiel, J. M.; and Tardós, J. D. 2021. Orb-slam3: An accurate open-source library for visual, visual-inertial, and multimap slam. *IEEE Transactions on Robotics*, 37(6): 1874–1890.
- Carlone, L.; and Calafiore, G. C. 2018. Convex relaxations for pose graph optimization with outliers. *IEEE Robotics and Automation Letters*, 3(2): 1160–1167.
- Carlone, L.; Tron, R.; Daniilidis, K.; and Dellaert, F. 2015. Initialization techniques for 3D SLAM: A survey on rotation estimation and its use in pose graph optimization. In *2015 IEEE international conference on robotics and automation (ICRA)*, 4597–4604. IEEE.
- Engel, J.; Koltun, V.; and Cremers, D. 2017. Direct sparse odometry. *IEEE transactions on pattern analysis and machine intelligence*, 40(3): 611–625.
- Forster, C.; Pizzoli, M.; and Scaramuzza, D. 2014. SVO: Fast semi-direct monocular visual odometry. In *2014 IEEE international conference on robotics and automation (ICRA)*, 15–22. IEEE.
- Handa, A.; Whelan, T.; McDonald, J.; and Davison, A. J. 2014. A benchmark for RGB-D visual odometry, 3D reconstruction and SLAM. In *2014 IEEE international conference on Robotics and automation (ICRA)*, 1524–1531. IEEE.
- Hartley, R.; and Zisserman, A. 2003. *Multiple view geometry in computer vision*. Cambridge university press.
- He, Y.; Zhao, J.; Guo, Y.; He, W.; and Yuan, K. 2018. PL-VIO: Tightly-coupled monocular visual-inertial odometry using point and line features. *Sensors*, 18(4): 1159.
- Joo, K.; Kim, P.; Hebert, M.; Kweon, I. S.; and Kim, H. J. 2021. Linear RGB-D SLAM for structured environments. *IEEE Transactions on Pattern Analysis and Machine Intelligence*, 44(11): 8403–8419.
- Kottas, D. G.; and Roumeliotis, S. I. 2013. Efficient and consistent vision-aided inertial navigation using line observations. In *2013 IEEE International Conference on Robotics and Automation*, 1540–1547. IEEE.
- Labbé, M.; and Michaud, F. 2019. RTAB-Map as an open-source lidar and visual simultaneous localization and mapping library for large-scale and long-term online operation. *Journal of Field Robotics*, 36(2): 416–446.

- Li, X.; He, Y.; Lin, J.; and Liu, X. 2020a. Leveraging planar regularities for point line visual-inertial odometry. In *2020 IEEE/RSJ international conference on intelligent robots and systems (IROS)*, 5120–5127. IEEE.
- Li, X.; Li, Y.; Örnek, E. P.; Lin, J.; and Tombari, F. 2020b. Co-planar parametrization for stereo-SLAM and visual-inertial odometry. *IEEE Robotics and Automation Letters*, 5(4): 6972–6979.
- Li, Y.; Brasch, N.; Wang, Y.; Navab, N.; and Tombari, F. 2020c. Structure-slam: Low-drift monocular slam in indoor environments. *IEEE Robotics and Automation Letters*, 5(4): 6583–6590.
- Li, Y.; Guo, Z.; Yang, Z.; Sun, Y.; Zhao, L.; and Tombari, F. 2024. Open-Structure: Structural Benchmark Dataset for SLAM Algorithms. *IEEE Robotics and Automation Letters*.
- Lu, Y.; and Song, D. 2015. Visual navigation using heterogeneous landmarks and unsupervised geometric constraints. *IEEE Transactions on Robotics*, 31(3): 736–749.
- McLean, G. F.; and Kotturi, D. 1995. Vanishing point detection by line clustering. *IEEE Transactions on pattern analysis and machine intelligence*, 17(11): 1090–1095.
- Mur-Artal, R.; Montiel, J. M. M.; and Tardos, J. D. 2015. ORB-SLAM: a versatile and accurate monocular SLAM system. *IEEE transactions on robotics*, 31(5): 1147–1163.
- Mur-Artal, R.; and Tardós, J. D. 2017. Orb-slam2: An open-source slam system for monocular, stereo, and rgb-d cameras. *IEEE transactions on robotics*, 33(5): 1255–1262.
- Paigwar, A.; Er kent, Ö.; Sierra-Gonzalez, D.; and Laugier, C. 2020. GndNet: Fast ground plane estimation and point cloud segmentation for autonomous vehicles. In *2020 IEEE/RSJ International Conference on Intelligent Robots and Systems (IROS)*, 2150–2156. IEEE.
- Qin, T.; Li, P.; and Shen, S. 2018. VINS-Mono: A Robust and Versatile Monocular Visual-Inertial State Estimator. *IEEE Transactions on Robotics*, 34(4): 1004–1020.
- Rosinol, A.; Abate, M.; Chang, Y.; and Carlone, L. 2020. Kimera: an open-source library for real-time metric-semantic localization and mapping. In *2020 IEEE International Conference on Robotics and Automation (ICRA)*, 1689–1696. IEEE.
- Salas-Moreno, R. F.; Glocken, B.; Kelly, P. H.; and Davison, A. J. 2014. Dense planar SLAM. In *2014 IEEE international symposium on mixed and augmented reality (ISMAR)*, 157–164. IEEE.
- Schonberger, J. L.; and Frahm, J.-M. 2016. Structure-from-motion revisited. In *Proceedings of the IEEE conference on computer vision and pattern recognition*, 4104–4113.
- Straub, J.; Freifeld, O.; Rosman, G.; Leonard, J. J.; and Fisher, J. W. 2017. The Manhattan frame model—Manhattan world inference in the space of surface normals. *IEEE transactions on pattern analysis and machine intelligence*, 40(1): 235–249.
- Wang, W.; Zhu, D.; Wang, X.; Hu, Y.; Qiu, Y.; Wang, C.; Hu, Y.; Kapoor, A.; and Scherer, S. 2020. Tartanair: A dataset to push the limits of visual slam. In *2020 IEEE/RSJ International Conference on Intelligent Robots and Systems (IROS)*, 4909–4916. IEEE.
- Yang, Y.; and Huang, G. 2019. Aided Inertial Navigation: Unified Feature Representations and Observability Analysis. In *2019 International Conference on Robotics and Automation (ICRA)*, 3528–3534.
- Yunus, R.; Li, Y.; and Tombari, F. 2021. Manhattanslam: Robust planar tracking and mapping leveraging mixture of manhattan frames. In *2021 IEEE International Conference on Robotics and Automation (ICRA)*, 6687–6693. IEEE.
- Zhang, G.; Lee, J. H.; Lim, J.; and Suh, I. H. 2015. Building a 3-D line-based map using stereo SLAM. *IEEE Transactions on Robotics*, 31(6): 1364–1377.
- Zhao, L.; Huang, S.; Yan, L.; and Dissanayake, G. 2015. A new feature parametrization for monocular SLAM using line features. *Robotica*, 33(3): 513–536.
- Zhou, H.; Zou, D.; Pei, L.; Ying, R.; Liu, P.; and Yu, W. 2015. StructSLAM: Visual SLAM with building structure lines. *IEEE Transactions on Vehicular Technology*, 64(4): 1364–1375.
- Zhou, L.; Koppel, D.; and Kaess, M. 2021. LiDAR SLAM with plane adjustment for indoor environment. *IEEE Robotics and Automation Letters*, 6(4): 7073–7080.
- Zou, D.; Wu, Y.; Pei, L.; Ling, H.; and Yu, W. 2019. StructVIO: Visual-inertial odometry with structural regularity of man-made environments. *IEEE Transactions on Robotics*, 35(4): 999–1013.
- Zuo, X.; Xie, X.; Liu, Y.; and Huang, G. 2017. Robust visual SLAM with point and line features. In *2017 IEEE/RSJ International Conference on Intelligent Robots and Systems (IROS)*, 1775–1782. IEEE.